Materials and Design 146 (2018) 125–133

Contents lists available at ScienceDirect

Materials and Design

journal homepage: www.elsevier.com/locate/matdes

Effect of particle shape and size on the morphology and optical properties of zinc oxide synthesized by the polyol method

T.E.P. Alves [a,b,*], C. Kolodziej [c], C. Burda [c], A. Franco Jr [d]

[a] Instituto Federal de Educação, Ciências e Tecnologia de Goiás, Anápolis, Goiás, Brazil
[b] Instituto de Química, Universidade Federal de Goiás, Goiânia, Goiás, Brazil
[c] Department of Chemistry, Case Western Reserve University, Cleveland, OH, United States
[d] Instituto de Física, Universidade Federal de Goiás, Goiânia, Goiás, Brazil

HIGHLIGHTS

- Polyol method was used to produce zinc oxide nanoparticles through decomposition of zinc acetate.
- Additional acetate ions influence the preferential growth of the crystal structure, altering the shape.
- Hydrolysis reaction time is used to control the particle size while retaining the shape.
- Shape, size, and defects affect optical properties, such as band-gap and photoluminescence.

GRAPHICAL ABSTRACT

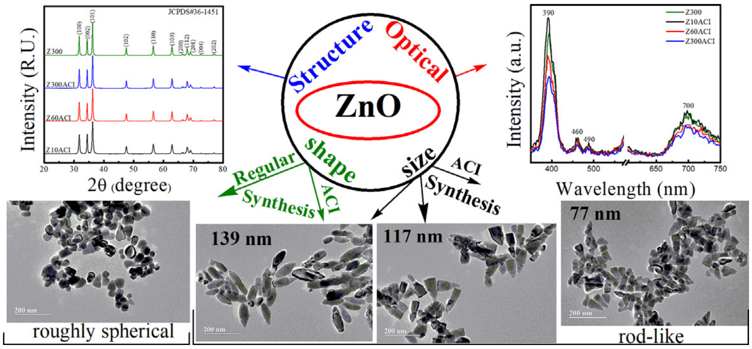

ARTICLE INFO

Article history:
Received 11 October 2017
Received in revised form 3 March 2018
Accepted 5 March 2018
Available online 6 March 2018

Keywords:
Polyol method
Zinc oxide
Control of shape and size
Optical properties
Defects

ABSTRACT

In this study we prepared zinc oxide (ZnO) nanoparticles using the polyol method with zinc acetate and/or sodium acetate in a propylene glycol medium with varied hydrolysis reaction time (10, 60 and 300 min). It was observed that the hydrolysis reaction time and the concentration of acetate ions had a strong effect on the morphology and size of ZnO nanoparticles (NPs). X-ray diffraction (XRD) patterns revealed that all samples crystalized in the typical ZnO wurtzite structure and Rietveld refinement was used to characterize the structure and to suggest a preferential growth. Fourier transformed infrared spectroscopy (FTIR) was performed and showed the typical ZnO band, no impurity signals, as well as differences in A_1 and E_1 vibration modes due to different crystal growth in the structure. Raman scattering was carried out to determine the defects in the structure of ZnO, such as interstitial oxygen and oxygen vacancies. Transmission electron microscope (TEM) images revealed that ZnO NPs size and shape are strongly dependent on the hydrolysis reaction time and addition of acetate counter ions, respectively. The change in shape and size has also affected the optical properties, such as the optical bandgap (E_g) of ZnO NPs and their florescence.

1. Introduction

Zinc oxide (ZnO) is a well-known non-toxic and chemically stable material used in numerous research areas such as gas sensors [1], photovoltaic devices [2], inks [3], catalysis [4], ultraviolet light emitting

---

[*] Corresponding author at: Instituto Federal de Educação, Ciências e Tecnologia de Goiás, Anápolis, Goiás, Brazil.
E-mail address: thiago.alves@ifg.edu.br (T.E.P. Alves).

https://doi.org/10.1016/j.matdes.2018.03.013
0264-1275/

diodes [5], dye-sensitized solar cells [6,7] and spintronics [8]. The broad development of ZnO is due to the wide direct band gap of 3.37 eV that is strongly affected by doping and exhibits a large exciton binding energy of 60 meV at room temperature. Moreover, ZnO crystalizes in a stable wurtzite structure with lattice parameter $a = 3.2495$ Å and $c = 5.2069$ Å in a hexagonal compact (hcp) structural arrangement, belonging to the $p6_3mc$ space group. ZnO hcp is an excellent host matrix for doping atoms, a feature that makes it a potential material to produce doped or composite semiconductors [9,10]. ZnO is often described as a material that is able to generate many intrinsic defects, either interstitial atoms or atomic vacancies, thus leading to changes in the electronic structure [11]. These defects can be leveraged to produce changes in the electronic structure and, combined with size and morphological control, drive ZnO NP research due to its strong influence on several important physical properties, especially optical properties.

The wurtzite structure of ZnO is a polar crystal where each Zn^{2+} ion is surrounded by four O^{2-} ions and has a large difference in electronegativity between Zn and O. In addition, The ZnO structure has a polar axis (c axis) which is positioned perpendicular to the basal plane contributing to the breaking of symmetry. These factors, combined with the thermodynamic and kinetic aspects, allow the occurrence of different growth rates in the crystalline faces, which can lead to preferential directions of growth along the various axes of the crystal [12]. In this sense, the chemical reactions are able to promote several thermodynamic environments to favor a certain direction of growth kinetics, and can be the key to success, guaranteeing the quality of the material through experimental control and confinement of desired size and shape due to strict control of the different rates of crystal growth [13].

ZnO has been produced with several morphologies through different methods, such as coprecipitation [14], molecular beam epitaxial (MBE) growth [15], chemical vapor deposition (CVD) [16], metallic organic chemical vapor deposition (MOCVD) [17], sol-gel process [18], combustion reaction [19], solvent-free synthesis [20], thermal decomposition [21] and the polyol method [22]. The polyol method can be described as a facile and inexpensive synthetic route and it does not need high temperatures, advanced equipment, or additive calcination steps. In general, its synthetic route uses polyol as solvent, for instance, ethylene glycol (EG), diethylene glycol (DG), propylene glycol (PPG) and a metallic acetate as precursor.

The polyol acts as a good agent to stabilize particle growth and agglomeration, further promoting the reduction of the metal in solution [23,24]. The polyol method is similar to the sol-gel synthesis, however, it has one fundamental difference, the forced hydrolysis phenomenon, i.e. a controlled amount of water is added to reactional media to reach the boiling point [26]. The controlled concentration of metallic ions and surfactants is very important to ensure good reproducibility in several approaches. Ultimately, these parameters are important for ZnO NP synthesis due to reduction of the metal oxides through controlled amounts of water, metal and surfactant to achieve high quality materials [27].

Interest in tunable physical properties through chemical reaction synthesis has been reported for ZnO and was performed with different approaches such as thermal annealing, control of growth for pure ZnO or using different dopants [22,28–30]. The role of the solvent and surfactant in the polyol method are reported in the literature and often well described and analyzed as fundamental factors influencing the size and shape of particles [31–33]. Although so much is known about the polyol method, the time of reflux still varies frequently in the literature, with several times between 2 and 12 h [30,34–36], showing a need for understanding of the effect of reflux time on NPs. In this work we

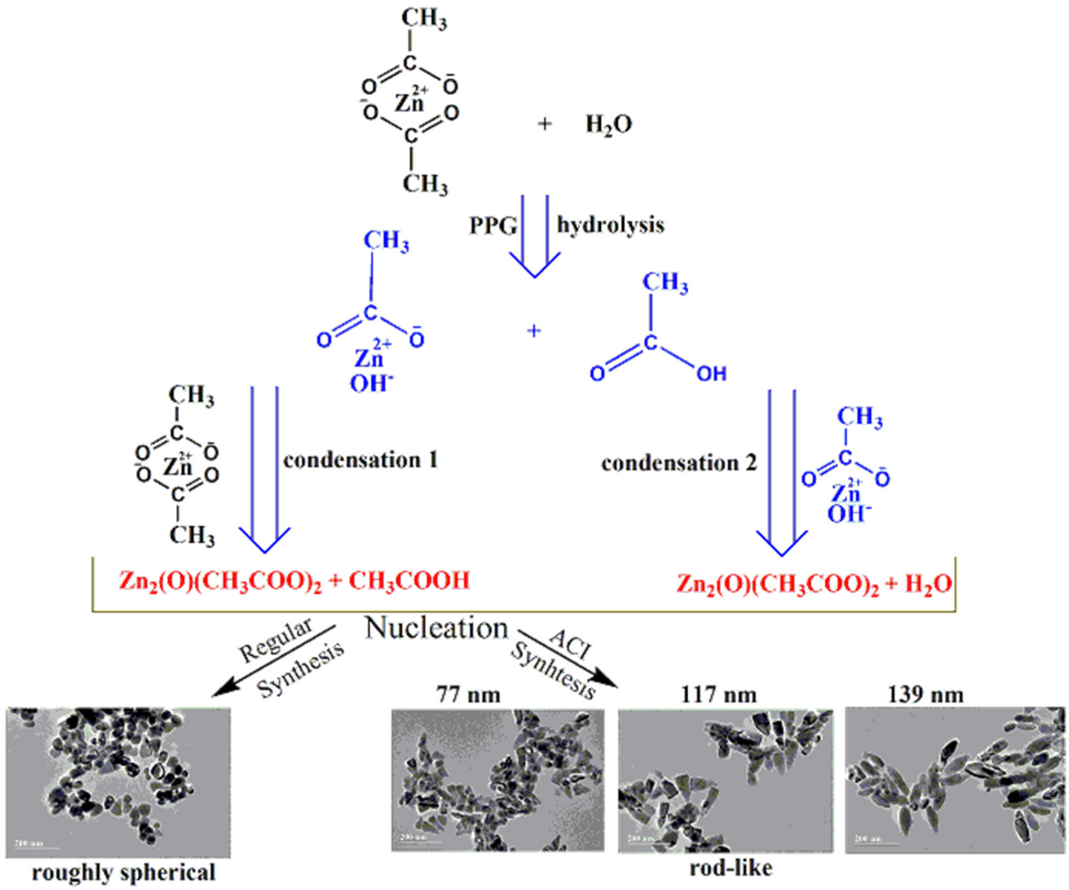

Fig. 1. Schematic representation of the steps of ZnO polyol synthesis as well as are showed the morphology aspects of particles from each synthesis.

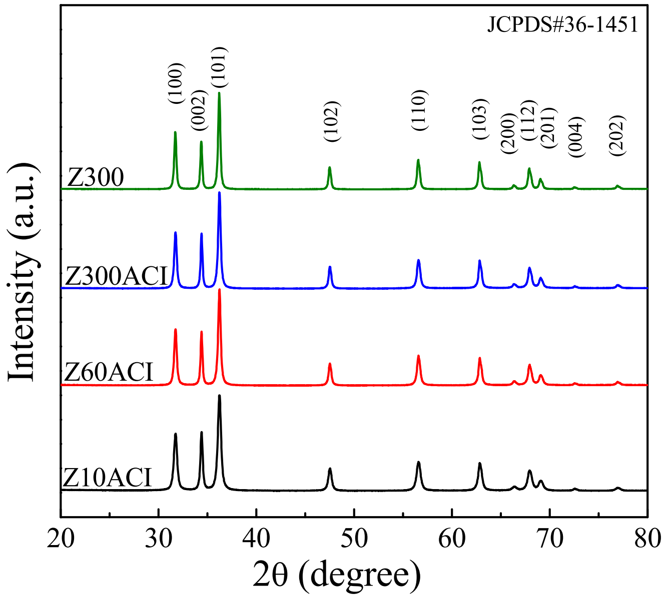

Fig. 2. X-ray diffraction patterns for all samples prepared by the Polyol method at room temperature.

have synthesized ZnO with controlled shape and size through the polyol method using two different approaches, studied the influence of additional counter ions (ACI) during reaction for formation of ZnO particles, and investigated the influence of hydrolysis reaction time. An additional amount of counter ion in solution strongly influences the shape of particles and changing hydrolysis reaction time controls particles size.

2. Experimental procedure

2.1. Synthesis

Analytical grade reagents, 1,2-propanodiol, propylene glycol (PPG, Aldrich), anhydrous sodium acetate (CH_3COONa, Aldrich), zinc acetate dihydrate ($(CH_3COO)_2Zn \cdot 2H_2O$, Aldrich) were used to synthesize ZnO. Two approaches will be discussed in this paper: particle shape control due to varying amounts of acetate counter ions (ACI) in solution, and particle size tuning due to different hydrolysis reaction time. In both cases, the pathway towards the final products is similar and can be summarized in two steps: (i) hydrolysis reaction and (ii) condensation reaction until the formation of a first seed nucleus. Hydrolysis reaction is a fundamental step of the reaction which relies on available water in the reaction media, otherwise the hydrolysis will fail and there will be no condensation reaction and no products. On the other hand, an excess of water could induce the formation of large particles and large distribution of sizes. In this sense, the precise hydration ratio is very important to the reaction and should be previous checked empirically to get an optimal value. The hydration ratio can be calculated through the simple ratio between the number of moles of zinc and number of moles of water, n_{ZnO}/n_{H2O} [26]. The condensation reaction can occur in two different ways, however, both are so reactive and thermodynamically favorable that there is not a significant difference in the final products of the reaction. A general schematic representation of polyol reaction is shown in Fig. 1 [37].

2.1.1. Regular synthesis of ZnO (Z300)

Zinc acetate was dissolved in 1,2-propanodiol with concentration 0.3 M of Zn in solution. The solution was stirred for 30 min to ensure homogeneity. Following, a precisely calculated amount of deionized water was added to promote hydrolysis. The amount of water must be carefully calculated, including all molecular content in hydrides of reactants. The hydration molar ratio used was 1:9. The homogenous medium was heated to the boiling point of 1,2-propanodiol (150 °C) with control rate of 3 °C/min, then, after 10 min of reflux, the solution became turbid and milk-like, and the reflux was kept for a total of 300 min. Then, the system was cooled and the as-prepared solution was centrifuged at 4000 rpm for 15 min to produce a nanoparticle precipitate and then washed several times with water and ethanol. Finally, the particles were dried at 80 °C for about 3 h in air atmosphere to obtain a thin white powder. This powder will be referred to as Z300.

2.1.2. Synthesis of ZnO with additional counter ions (ZACI)

Similarly, zinc acetate was dissolved in 1,2-propanodiol (0.3 M), and the solution was stirred for 30 min with deionized water in a 1:9 hydration ratio to promote hydrolysis. The fundamental difference in the ACI approach was an addition of excess acetate counter ions added as anhydrous sodium acetate with a molar ratio of 1:3 zinc:sodium. The

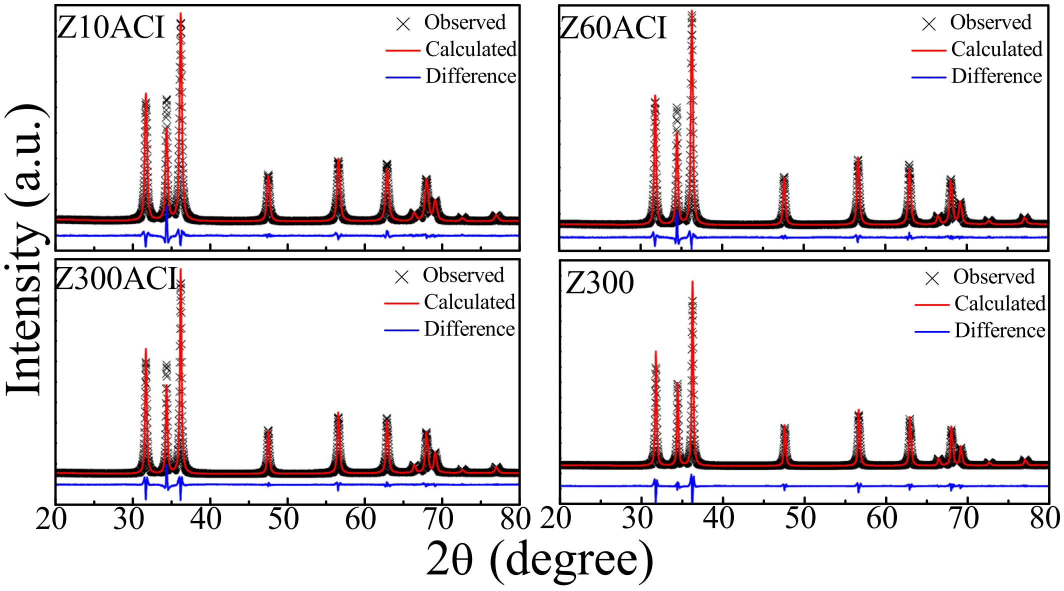

Fig. 3. Rietveld refinement for samples calculated by the equiaxial model.

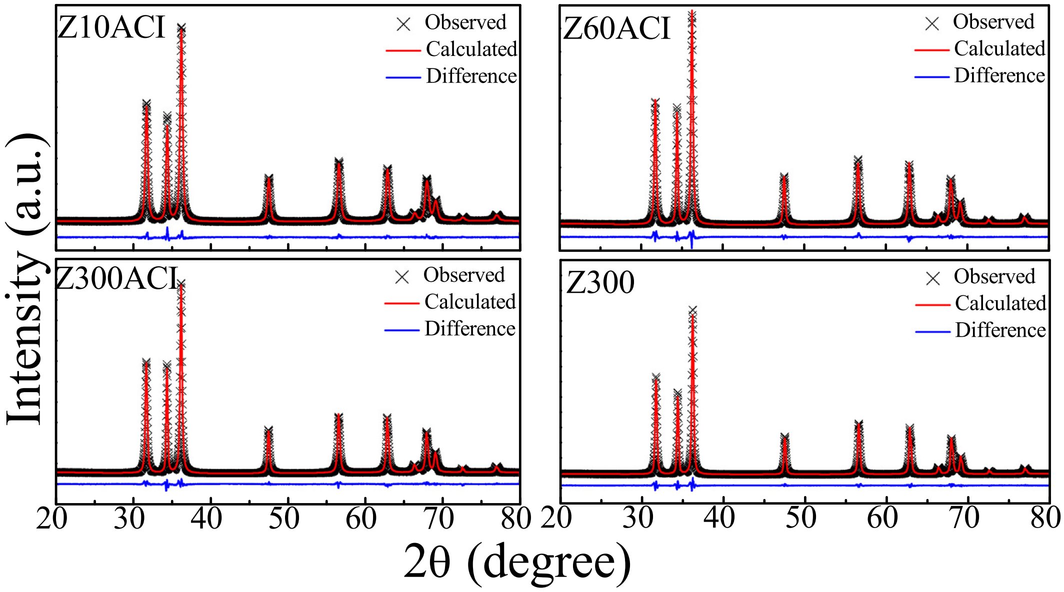

Fig. 4. Rietveld refinement for samples calculated by the uniaxial model.

solution became turbid and milk-like after 10 min of reflux, following the same protocol to precipitate and wash samples. The reflux time was varied, producing three sets of samples under 10, 60 and 300 min of reflux, referred to as Z10ACI, Z60ACI, Z300ACI, respectively.

2.2. Characterization

Particle size distribution and morphology of all samples were performed on a JEOL Transmission Electron Microscope (TEM) (model JEM 2100) working at 200 kV. Samples were dispersed in ethanol and sonicated for 5 min and droplets of this dispersion were placed onto a copper grid coated with parlodion and carbon films and dried in air. The crystalline structure was analyzed through X-ray diffraction (XRD) using a Shimadzu 6000 diffractometer with CuKα radiation ($\lambda = 1.5418$ Å) for a range of Bragg angles ($20° \le 2\theta \le 80°$) with a scanning rate of 2°/min and 3 s dwell time at room temperature. The crystalline phases were identified by using X-Pert HighScore (Panalytical) software and the crystallography data for all samples were obtained by using the Inorganic Crystal Structure Database (ICSD), and the Rietveld refinement method was performed using General Structure Analysis Software-II (GSAS-II) software. The infrared spectra (FT-IR) were collected using a Perkin-Elmer Spectrum System 400 with samples in KBr pellets (1%) in the range of 400–4000 cm^{-1}. Diffuse reflectance spectra were obtained by using an UV/VIS/Near IR spectrometer (Perkin-Elmer Lambda, model 1050) equipped with the praying mantis accessory in the range of 250 − 800 nm. For this experiment, barium sulfate ($BaSO_4$) powder was used as reference material. Florescence measurements were performed on a Varian Cary Eclipse Fluorescence Spectrophotometer with an excitation wavelength for all samples of $\lambda_{exc} = 290$ nm. Raman spectroscopy was performed on a Bruker Sentinel with an excitation of wavelength of 785 nm at 70 mW and five co-adds with 60 s of integration time.

3. Results and discussion

XRD patterns of all samples obtained at room temperature are displayed in Fig. 2, which showed the formation of typical wurtzite structures (JCPDS PDF no. 36-1451 diffraction pattern card). Even though all samples show the same ZnO hcp structure, the diffractograms reveal a difference between intensities in the (002) diffraction peaks, mainly for ACI samples, which is evidence for preferential growth along the *c*-axis [22]. Rietveld refinement was employed to investigate the structural differences and preferential growth [38,39]. Refinement was performed through two different mathematic input functions. First the equiaxial model, which considers symmetric growth for all crystalline directions, then the uniaxial model, which considers specific growth through one preferential direction. For our samples, the preferential direction considered was 002 [38]. The refined graphs are shown in Figs. 3 and 4, where discrepancies can be seen between the calculated and experimental results for the equiaxial model, mainly in the ACI samples. However, there is good agreement between the calculated and experimental patterns under the uniaxial refinement model, which can indicate different directions of growth for our samples. For instance, the values of the refinement parameters (Rp, Rwp and GOF) shown in Table 1 are higher for the equiaxial refinement than the uniaxial refinement. The GOF is the ratio between calculated and experimental diffraction data, with 1 being an ideal value indicating the quality of refinement. To verify the preferential growth direction of the ZnO structure, the x-ray diffractograms were analyzed using two approaches. First, the difference between particles' size corresponding to the three most intense peaks were calculated using the Scherrer

Table 1
Fitted data for samples through equiaxial and uniaxial models.

	Samples refinement equiaxial				Samples refinement uniaxial (002)			
Parameter	Z300	ZACI10	ZACI60	ZACI300	Z300	ZACI10	ZACI60	ZACI300
Rp%	9.6	18.2	14.8	15.4	5.6	6.8	5.7	6.9
Rwp%	12.1	21.4	17.4	14.9	4.8	7.1	6.3	5.3
GOF	3.95	9.88	8.65	9.45	1.61	1.82	1.74	1.69

Table 2
Scherrer diameter and ratio I_{100}/I_{002} for all samples.

Parameter	Samples			
	Z10ACI	Z60ACI	Z300ACI	Z300
I_{100}/I_{002}	1.01	0.96	0.98	0.82
D(100) nm	21	27	27	37
D(002) nm	32	44	46	39
D(101) nm	23	30	30	36

equation, $D_{hkl} = \frac{k\alpha}{(\beta_{hkl}\cos\theta)}$ where D_{hkl} is the crystallite size for the peak, K is a numerical factor referred to as the crystallite-shape factor, λ is the wavelength of the X-rays, β_{hkl} is the full-width at half-maximum for each peak (FWHM) of the x-ray diffraction peak in radians and θ is the Bragg angle [40]. In addition, the ratio between the integrated intensities I_{100}/I_{002} also was calculated, the values found can be seen in Table 2 [30]. The Scherrer diameter is quite close to the regular sample Z300 for all peaks considered, whereas the ACI samples showed discrepancies related to peak 002. It is in agreement of the ratio values (I_{100}/I_{002}) found for the ACI and regular samples, approximately 1 and 0.8, respectively. It may be due to a larger growth along *c*-axis for ACI samples than the regular sample Z300 caused for the additional acetate counter ions in excess during reaction.

FTIR measurements for precursors in solution were analyzed to investigate the reaction in situ during reflux. Thus, aliquots were taken several times from the reaction reflux of the solution at different temperatures and reaction times. For instance, precursor solution (all reagents mixed at room temperature), 100 °C (aliquot extracted at 100 °C) and 150 °C (aliquot extracted at 150 °C), 150 °C_10 min and 150 °C_60 min (both extracted during reflux at 150 °C after 10 min and 60 min, respectively), see Fig. 5. All FTIR spectra (Fig. 5) showed a band at 3400 cm^{-1} which can be assigned to the O—H stretching vibration to the –OH groups. Some bands in the interval from 2800 cm^{-1} to 2950 cm^{-1} can be attributed to the C—H bonds from $-CH_2-$ and $-CH_3$ groups. The weak bands in the range 1400 cm^{-1}–1450 cm^{-1} corresponding to the bending vibration of CH_2 and CH groups. The region 1150–1000 cm^{-1} is characterized by the vibration frequency of the –OH groups. These mentioned bands are related mainly to the 1,2-propanodiol structure, which was used as solvent in the precursor solution and its presence is too higher than other ones. It is possible to observe another band in the 1580 cm^{-1} that correspond to the symmetric stretching vibration modes of COO^{-} group due to the presence of acetate precursor [11,21,22,32]. The sample precursor solution spectrum at 150 °C did not show any change, however, for the samples at 150 °C after 10 min of reflux, a characteristic ZnO vibrational mode arise around 450 cm^{-1} evidencing the quickly formation of nanoparticles [41]. ZnO washed powders were submitted to FTIR to investigate the sample's purity and to observe the formation of ZnO bonds in Fig. 6. Spectra of washed samples show that the powders are free from impurities as well as exhibit typical vibrational modes of ZnO bonds already mentioned. According the rules of symmetry, the ZnO structure belongs to the p6_3*mc* space group and should show 8 vibrational modes; $\Gamma = 2A_1 + 2E_1 + 2B_1 + 2E_2$, however, A_1 and E_1 are acoustic vibrational modes, and B_1 is a Raman silent vibrational mode. Therefore,

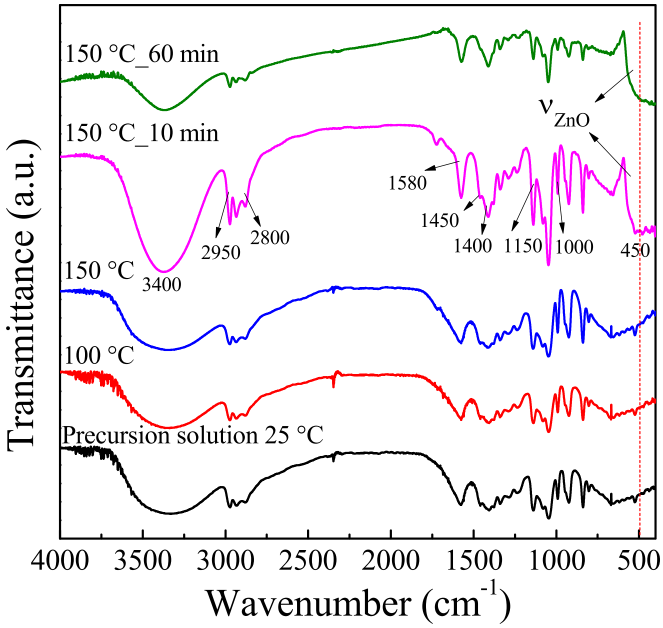

Fig. 5. FTIR for several aliquots of precursor solution, during heating from room temperature to 150 °C (reflux temperature) and during reflux after 10 and 60 min, respectively.

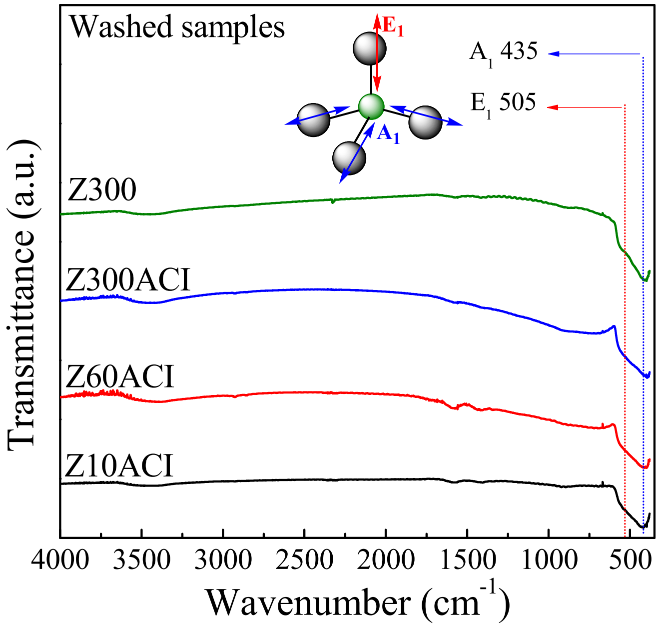

Fig. 6. FTIR for samples regular and ACI synthesis at room temperature. Inset shows the difference between A_1 and E_1 modes for ZnO wurtzite.

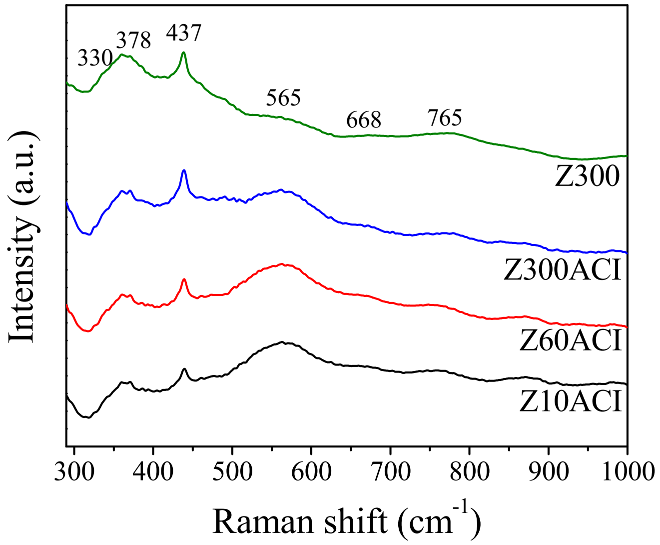

Fig. 7. Raman spectroscopy of Z10ACI, Z60ACI, Z300ACI, and Z300 at room temperature.

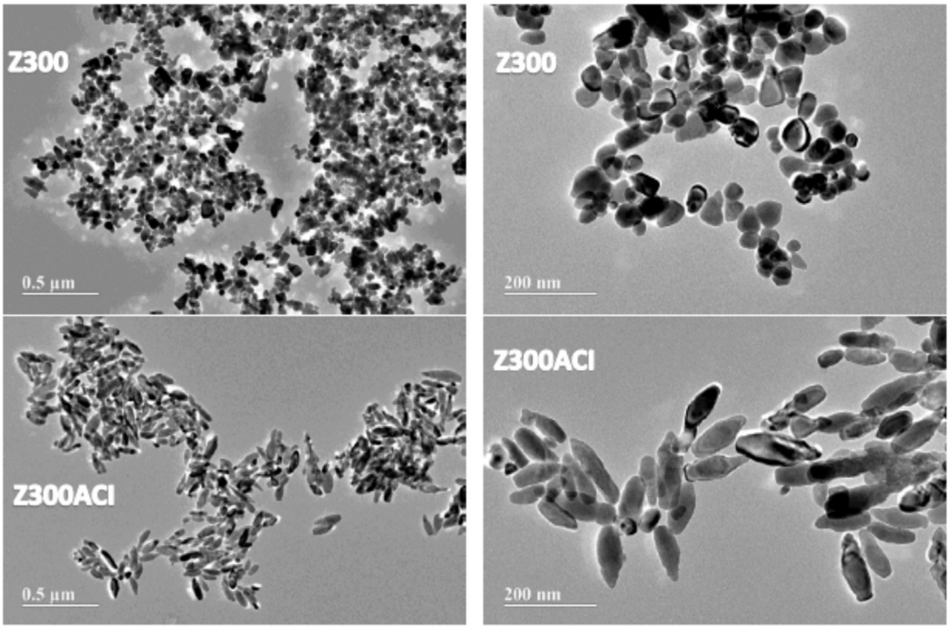

Fig. 8. TEM of samples at the same hydrolysis reaction time (300 min) with different additional counter ions to evidence the difference in shape of the NPs.

the predicted active Raman modes for this structure are A_1, E_1 and $2E_2$, and active infrared modes A_1 and E_1 [42]. Furthermore, specifically for ZnO, it is possible to observe longitudinal (LO) and transversal (TO) modes due to its polar structure, but only LO modes can be measured between 400 and 4000 cm^{-1}. The A_1 vibration mode (LO) is related with the vibrational energetic transition on ZnO chemical bond parallel to the *c*-axis while E_1 (LO) is related with the chemical bonds perpendicular to the *c*-axis [11]. Differences between the vibrational modes provide strong evidence to attribute the existence of these two active modes at 437 cm^{-1} cm and 505 cm^{-1} to A_1 and E_1, respectively. Thus, it is easy to notice that E_1 and A_1 intensities are slight closer for ACI samples than for the regular Z300 sample. This might agree by the different

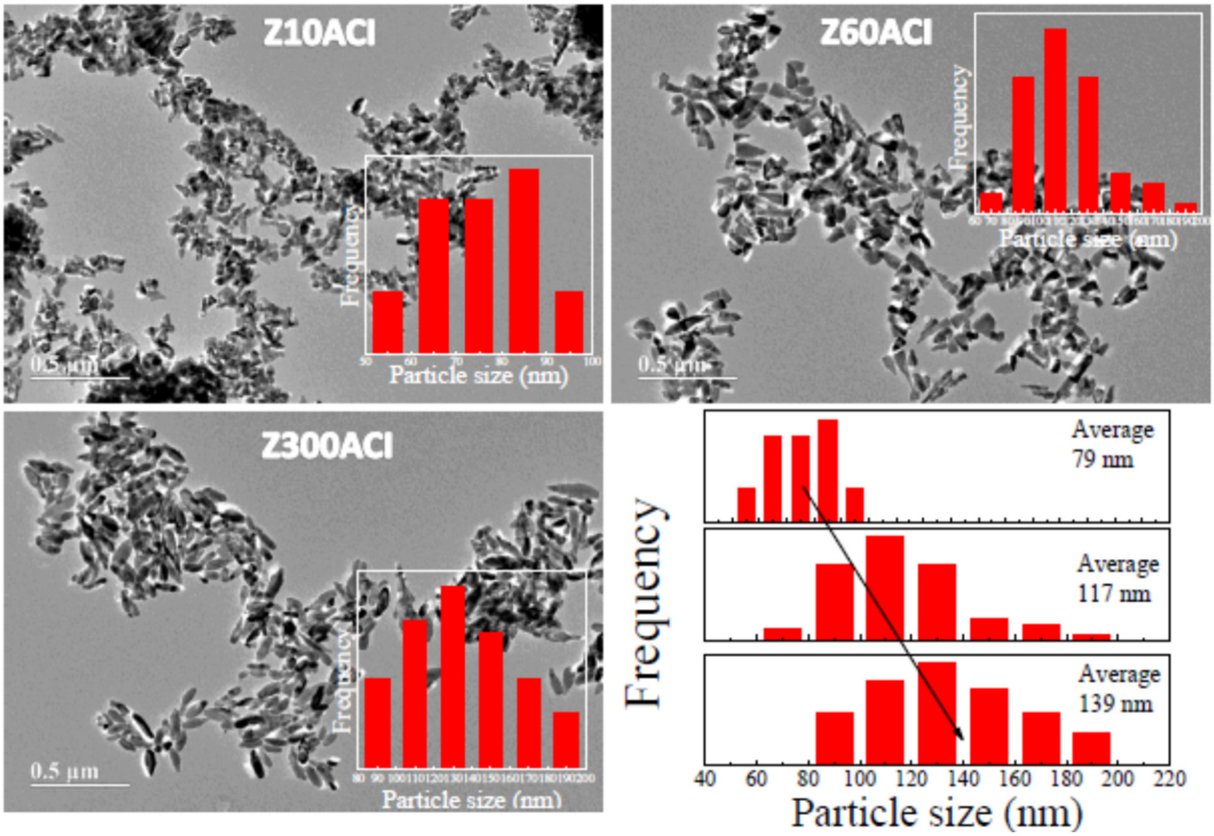

Fig. 9. TEM of samples synthesized with the same additional (ACl) counter ions showing size control through hydrolysis reaction time; 10 min, 60 min and 300 min, respectively.

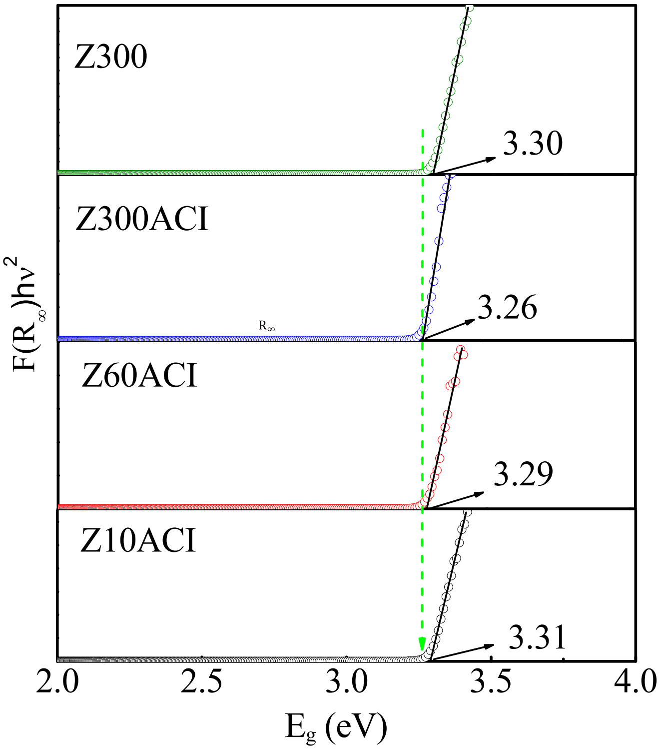

Fig. 10. Direct band gap (E_g) for all samples, determined by diffuse reflectance.

number of bonds parallel and perpendicular to atoms in the basal plane, and could be related to growth in the perpendicular direction throughout the *c*-axis observed through XRD.

Room temperature Raman spectra of ZnO nanopowders for all samples are shown in Fig. 7. Based on the previous discussion about symmetrical Raman mode scattering, there are A_1, E_1 and $2E_2$, where A_1 and E_1 are polar modes and $2E_2$ (E_2^{low} and E_2^{high}) nonpolar modes. A_1 and E_1 polar modes split into TO (A_1 TO and E_1 TO) and LO (A_1 LO and E_1 LO) components, and E_2 nonpolar modes, low and high, are associated with the vibration of the Zn sublattice and oxygen atoms, respectively [43]. The characteristic peak for ZnO is present in all spectra around 437 cm^{-1} and might be related to the E_2 non-polar optical phonon mode of the wurtzite ZnO crystal, corresponding to the oxygen atoms. The intensities of these peaks are frequently attributed to the crystallization of the structure [44]. In this sense, it is easy to see that samples with ACI tend to show smaller intensities than regular samples, thus the crystallization of ACI samples were influenced by the presence of excess acetate counter ions in solution during crystallization as well as the hydrolysis reaction time. Raman scattering measurements were carried out in a backscattering geometry using an npolarized light, thereby allowing only E_2, A_1 (TO), and E_1 (TO) modes for incident radiation perpendicular to the *c*-axis of the sample, and E_2 and A_1 (LO) for incident light parallel to the *c*-axis. ZnO NPs were measured as a powder, which provides a random orientation of the crystals. Because of this, Raman cannot be used to determine growth orientation for these powders [45]. The mode at 330 cm^{-1} is ascribed to the difference $E_2^{\text{high}} - E_2^{\text{low}}$, peaks at 668 cm^{-1} and 765 cm^{-1} are related to multiple phonon scattering, the peak at 378 cm^{-1} corresponds to A_1 (TO) mode, and the broad peak at 565 cm^{-1} corresponds to the A_1 (LO) mode [43]. The A_1 (LO) mode is strongly related mainly to the presence of oxygen interstitial defects throughout the structure [43,45].

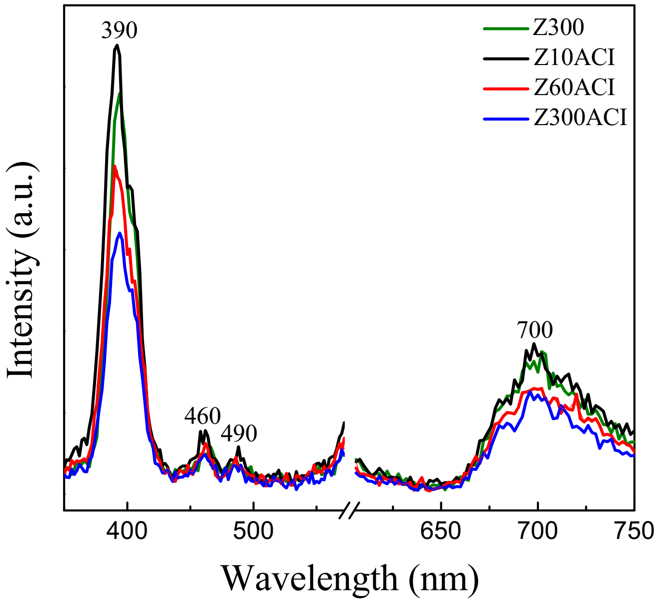

Fig. 11. Room temperature photoluminescence spectra for all samples excited at 585 nm. The break in the x-axis is to eliminate signal from the excitation source.

Transmission electron microscope (TEM) images revealed different morphology, shape and sizes of the particles. ACI samples do not have a similar shape to the NPs from regular synthesis. The regular synthesis showed roughly spherical nanoparticles and the ACI synthesis showed rod-like particles, when compared to samples with the same reflux time (Fig. 8). However, size changes can be seen for the ACI particles as the hydrolysis reaction time (HRT) is varied. For a HRT of 10, 60 and 300 min, we found an average size of 79, 117 and 139 nm, respectively (Fig. 9).

The UV-VIS absorption related to the transition of electrons from valence to conduction band was used to determine the optical bandgap (E_g) of the nanoparticles. E_g values of all samples were calculated based on diffuse reflectance using the Tauc plot [46] modeled by $(h\nu\alpha)^{1/n} = A(h\nu - E_g)$, where α is the absorption coefficient, $h\nu$ is the incident photon energy, E_g is the band gap energy, and A is a constant. The variable n is related to the type of transition and can assume several values depending on the desired transition, for instance, $n = 1/2, 3/2, 2,$ and 3 for direct allowed, direct forbidden, indirect allowed and indirect forbidden transitions, respectively. The Kubelka-Munk model [47] was used to transform reflectance data by $\alpha = \mathrm{F}(\mathrm{R}_\infty) = \frac{(1-\mathrm{R}_\infty)^n}{2\mathrm{R}_\infty}$, where R_∞ is the ratio between the sample's reflectance and reference's reflectance (barium sulfate was used as a reference). Thus combining the Tauc plot and Kubelka-Munk model, the equation becomes $\mathrm{F}(\mathrm{R}_\infty) = \frac{A(h\nu - Eg)^n}{h\nu}$, where $n = 1/2$ for direct allowed transition. E_g for each sample was obtained by extrapolating the linear part of the plot of $[\mathrm{F}(\mathrm{R}_\infty)h\nu]^{1/2}$ vs. $h\nu$ for where $h\nu$ is equal to zero and the results are displayed in Fig. 10. The average E_g values for these samples are around 3.28 eV, which is slightly lower than the ZnO bulk bandgap of 3.37 eV [11]. When the dimension of particles becomes smaller, the quantum effects and surface phenomenon can strongly influence the E_g [48]. It is possible to notice a slight variation to the E_g values mainly for the rod-like ACI particles, from 3.26 to 3.31 eV, for Z300ACI and Z10ACI, respectively. It can be examined by Brus' quantum confinement model, as well as intrinsic defects of oxygen in interstitial sites of ZnO could cause this kind of behavior [49,50].

Fig. 11 shows the room temperature photoluminescence (PL) spectra for all ZnO samples measured with an excitation wavelength of 290 nm. It is well known that ZnO has an emission band around 390 nm in the ultra violet (UV) which is frequently considered a characteristic ZnO emission, attributed to the band–edge transition or exciton recombination [11,51]. Additionally, different visible emission bands have been reported for ZnO such as green, yellow-orange, blue and red, related to intrinsic and extrinsic defects present in the ZnO structure and many contributions have been made to explain these emissions.

For instance, green emission could be associated with a transition between singly ionized oxygen vacancies and photoexcited holes [52]. The yellow-orange emissions have been assigned to interstitial oxygen dislocation, as well as lithium dopants [11,53]. The blue emission has been reported to be related to interstitial zinc defect levels as initial states [54]. The red emission has been explained through the presence of oxygen interstitials and oxygen vacancies [55].

For our samples, it is possible to observe the characteristic sharp UV emission band at 390 nm, as two small blue emissions around 460 nm and 490 nm, and a broad red emission band centered at 700 nm. The samples synthesized with different HRT showed different intensities of the peak in 390 nm, it is evident that the different size of particles have influence in these intensities. The smaller particles have the bigger intensities for the UV peak [30]. The FTIR and energy dispersive x-ray spectroscopy (EDS) suggest that our washed samples are free of impurities. Therefore, the visible emission should correspond only to intrinsic defects. Due to a relatively small size, the particles have a large surface/volume ratio, which can produce some defects such as oxygen vacancies and oxygen interstitials. Thus, the blue emissions may be caused by a small amount of interstitial and oxygen vacancy defects of zinc to produce trap levels between the valence and conduction bands [49]. The red emission are related to the interstitial oxygen throughout the ZnO structure, as the Raman measurements are able to support.

4. Conclusions

We studied the synthesis of ZnO powders using the polyol method with different approaches: the regular synthesis, and with the presence of excess acetate counter ions. We showed that it was possible to control the shape and size of particles through these approaches. The XRD was used to characterize the structure and Rietveld refinement for the samples suggest a preferential growth in the *c*-axis direction through 002 planes and polar face, mainly for ACI samples under the influence of counter ions. By FTIR, the quick formation of the first nucleus was observed during reflux at around 10 min, and showed that the samples were free of impurities and byproducts. In addition, it was possible to differentiate A_1 and E_1 specific modes of vibration for ZnO, in agreement with the expected modes. Room temperature Raman spectra showed typical modes for ZnO around 437 cm^{-1} and the important broad band around 565 cm^{-1} attributed to interstitial oxygen and oxygen vacancies. TEM confirmed the control of shape for the same hydrolysis reaction time, and for the regular and ACI synthesis. The control of particles size for the same synthesis method and different hydrolysis reaction times resulting in 79, 117, and 139 nm average diameters for Z10ACI, Z60ACI and Z300ACI, respectively. Diffuse reflectance UV–Vis spectra were used to determine E_g, which were found to vary mainly for the ACI rod-like particles, from 3.26 to 3.31 eV, for Z300ACI and Z10ACI, respectively. Finally, the PL spectrum showed the typical band around 390 nm attributed to exciton recombination, blue emission related to defects as zinc interstitial and oxygen vacancy, and red emission corresponding to oxygen interstitials. We have shown the effect of reflux time to contribute greatly to the size of NPs and the influence of ACI on the preferred crystal growth orientation. These findings offer a better understanding of ZnO NP synthesis that can be readily utilized for semiconductors, photovoltaics, catalysis, ultraviolet light emitting diodes, amongst other applications.

Acknowledgements

Coordination for the Improvement of Higher Education Personnel – CAPES – Brazil by the financial support to the Ph.D. exchange student through the *Programa de Doutorado-sanduíche no Exterior* (PDSE-CAPES, process No. 88881.131531/2016-01). Federal Institute of Education, Science and Technology of Goiás - IFG through the *Programa de Apoio à Produtividade em Pesquisa* (PROAPP-2015/2016). Institute of Chemistry and Physics, Federal University of Goiás, Brazil and the Department of Chemistry, Case Western Reserve University, USA. One of us (A. F. Jr) is a CNPq fellow under Grant No. 308183/2012-6.

References

[1] C.S. Rout, A.R. Raju, A. Govindaraj, C.N.R. Rao, Ethanol and hydrogen sensors based on ZnO nanoparticles and nanowires, J. Nanosci. Nanotechnol. 7 (2007) 1923–1929, https://doi.org/10.1166/jnn.2007.742.

[2] S.K.N. Ayudhya, P. Tonto, O. Mekasuwandumrog, V. Pavarajarn, P. Praserthdam, Solvothermal synthesis of ZnO with various aspect ratios using organic solvents, Cryst. Growth Des. 6 (2006) 2446–2450, https://doi.org/10.1021/cg050345z.

[3] K.S. Suganthi, et al., Flex. Print. Electron. 3 (2018), 015001. https://doi.org/10.1088/2058-8585/aaa166.

[4] W. Xie, Z. Yang, H. Chun, Catalytic properties of lithium-doped ZnO catalysts used for biodiesel preparations, Ind. Eng. Chem. Res. 46 (2007) 7942–7949, https://doi.org/10.1021/ie070597s.

[5] D.P. Liu, G.D. Li, Y. Su, J.S. Chen, Highly luminescente ZnO nanocrystals stabilized by ionic-liquid components, Angew. Chem. Int. Ed. 45 (2006) 7370–7373, https://doi.org/10.1002/anie.200602429.

[6] H. Kind, H.Q. Yan, B. Messer, M. Law, P.D. Yang, Nanowire ultraviolet photodetectors and optical switches, Adv. Mater. 14 (2002) 158–160, https://doi.org/10.1002/1521-4095.

[7] N. Mir, M.S. Niasari, F. Davar, Preparation of ZnO nanoflowers and Zn glycerolate nanoplates using inorganic precursors via a convenient rout and application in dye sensitized solar cells, Chem. Eng. J. 181–182 (2012) 779–789, https://doi.org/10.1016/j.cej.2011.11.085.

[8] S.A. Wolf, D.D. Awschalom, R.A. Buhrman, J.M. Daughton, S. Von Molnar, M.L. Roukes, A.Y. Chtchelkanova, D.M. Treger, Spintronics: a spin-based electronics, Science 294 (2001) 1488–1495, https://doi.org/10.1126/science.1065389.

[9] Ü. Özgür, I. Ya, C. Liu Alivov, A. Teke, M.A. Reshchikov, A compressive review of ZnO material and devices, J. Appl. Phys. 98 (2005), 041301. https://doi.org/10.1063/1.1992666.

[10] M. Hassanpour, H.S. Hojaghan, M.S. Niasari, Degradation of methylene blue and Rhodamine B as water pollutants via green synthesized Co_3O_4/ZnO nanocomposite, J. Mol. Liq. 229 (2017) 293–299, https://doi.org/10.1016/j.molliq.2016.12.090.

[11] A. Sahai, N. Goswami, Probing the dominance of interstitial oxygen defects in ZnO nanoparticles through structural and optical characterizations, Ceram. Int. 40 (2014) 14569–14578, https://doi.org/10.1016/j.ceramint.2014.06.041.

[12] W.J. Li, E.W. Shi, W.Z. Zhong, Z.W. Yin, Growth mechanism and growth habit of oxide crystals, J. Cryst. Growth 203 (1999) 186–196, https://doi.org/10.1016/S0022-0248(99)00076-7.

[13] J. Zhang, L. Sun, J. Yin, H. Su, C. Liao, C. Yan, Control of ZnO morphology via a simple solution route, Chem. Mater. 14 (2002) 4172–4177, https://doi.org/10.1021/cm020077h.

[14] J.H. He, S.L. Yuan, Z.M. Tian, Y.S. Yin, P. Li, Y.Q. Wang, K.L. Liu, S.J. Yuan, X.L. Wang, L. Liu, Magnetic properties en Fe-doped NiO synthesized by co-precipitation, J. Magn. Magn. Mater. 320 (2008) 3293–3296, https://doi.org/10.1016/j.jmmm.2008.06.028.

[15] K. Iwata, P. Fons, A. Yamada, K. Matsubara, S. Niki, Nitrogen-induced defects in ZnO: N grown on sapphire substrate by gas source MBE, J. Cryst. Growth 209 (2000) 526–531, https://doi.org/10.1016/S0022-0248(99)00613-2.

[16] J.J. Liu, M.H. Yu, W.L. Zhou, Fabrication of Mn-doped ZnO diluted magnetic semiconductor nanostructures by chemical vapor deposition, J. Appl. Phys. 99 (2006), 08M119. https://doi.org/10.1063/1.2173235.

[17] T. Yang, J. Bian, H. Liang, J. Sun, X. Wang, W. Liu, Y. Chang, G. Du Yuchun, High quality p-type ZnO films grown by low pressure plasma-assisted MOCVD with N_2O rf plasma doping source, J. Mater. Process. Technol. 204 (2008) 481–485, https://doi.org/10.1016/j.jmatprotec.2008.03.007.

[18] A.K. Srivastava, M. Deepa, N. Bahadur, M.S. Goyat, Influence of Fe doping on nanostructures and photoluminescence of sol–gel derived ZnO, Mater. Chem. Phys. 114 (2009) 194–198, https://doi.org/10.1016/j.matchemphys.2008.09.005.

[19] A. Franco Jr, H.V.S. Pessoni, Enhanced dielectric constant of Co-doped ZnO nanoparticulate powders, Physica B 476 (2015) 12–18, https://doi.org/10.1016/j.physb.2015.07.004.

[20] M. Goudarzi, M.M. Kamazani, M.S. Niasari, Zinc oxide nanoparticles: solvent-free synthesis, characterization and application as heterogeneous nanocatalyst for photodegradation of dye from aqueous phase, J. Mater. Sci. Mater. Electron. 28 (2017) 8423–8428, https://doi.org/10.1007/s10854-017-6560-z.

[21] N. Mir, et al., Synthesis and characterization of ZnO nanohemispheres via solution-phase thermal decomposition and its comparison with the solid-phase approach, J. Ind. Eng. Chem. 21 (2015) 884–888, https://doi.org/10.1016/j.jiec.2014.04.027.

[22] S. Lee, S. Jeong, D. Kim, S. Hwang, M. Jeon, J. Moon, ZnO nanoparticles with controlled shapes and sizes prepared using a simple polyol synthesis, Superlattice. Microst. 43 (2008) 330–339, https://doi.org/10.1016/j.spmi.2008.01.004.

[23] S. Zinatloo-Ajabshir, et al., Facile fabrication of $Dy_2Sn_2O_7$-SnO_2 nanocomposites as an effective photocatalyst for degradation and removal of organic contaminants, J. Colloid Interface Sci. 497 (2017) 298–308, https://doi.org/10.1016/j.jcis.2017.03.031.

[24] M.S. Morassaei, et al., $Nd_2Sn_2O_7$ nanostructures: New facile Pechini preparation, characterization, and investigation of their photocatalytic degradation of methyl orange dye, Adv. Powder Technol. 28 (2017) 697–705, https://doi.org/10.1016/j.apt.2016.11.017.

[26] L. Poul, S. Ammar, N. Jouini, F. Fievet, F. Villain, Synthesis of inorganic compounds (metal, oxide and hydroxide) in polyol medium: a versatile route related to the sol-gel process, J. Sol-Gel Sci. Technol. 25 (2003) 261–265, https://doi.org/10.1023/A:1020763402390.

[27] M. Niederberger, N. Pinna, Metal Oxide Nanoparticles in Organic Solvents: Synthesis, Formation, Assemby and Application, first ed. Springer, 2009.

[28] K.S. Babu, A.R. Reddy, C. Sujatha, K.V. Reddy, Optimization of UV emission intensity of ZnO nanoparticles by changing the excitation wavelength, Mater. Lett. 99 (2013) 97–100, https://doi.org/10.1016/j.matlet.2013.02.079.

[29] K.S. Babu, A.R. Reddy, C. Sujatha, K.V. Reddy, A.N. Mallika, Annealing effects on photoluminescence of ZnO nanoparticles, Mater. Lett. 110 (2013) 10–12, https://doi.org/10.1016/j.matlet.2013.07.114.

[30] A. Dakhlaoui, M. Jendoubi, L.S. Smiri, A. Kanaev, N. Jouini, Synthesis, characterization and optical properties of ZnO nanoparticles with controlled size and morphology, J. Cryst. Growth 311 (2009) 3989–3996, https://doi.org/10.1016/j.jcrysgro.2009.06.028.

[31] M. Masjedi-Arani, M. Salavati-Niasari, A simple sonochemical approach for synthesis and characterization of Zn_2SiO_4 nanostructures, Ultrason. Sonochem. 29 (2016) 226–235, https://doi.org/10.1016/j.ultsonch.2015.09.020.

[32] M. Yousefi, et al., A facile room temperature synthesis of zinc oxide nanostructure and its influence on the flame retardancy of poly vinyl alcohol, J. Clust. Sci. 25 (2014) 397–408, https://doi.org/10.1007/s10876-013-0618-8.

[33] M.S. Morassaei, et al., New facile synthesis, structural and photocatalytic studies of $NdOCl$-$Nd_2Sn_2O_7$-SnO_2 nanocomposites, J. Mol. Liq. 220 (2016) 902–909, https://doi.org/10.1016/j.molliq.2016.05.041.

[34] A. Anzlovar, K. Kogej, Z.C. Orel, M. Zigon, Polyol mediated nano size zinc oxide and nanocomposites, Express Polym Lett 5 (2011) 604–619, https://doi.org/10.3144/expresspolymlett.2011.59.

[35] P. Nithiya, C. Shilpachakra, C. Ashok, Synthesis of TiO_2 and ZnO nanoparticles by facile polyol method for the assessment of possible agents for seed germination, Mater. Today Proc. 2 (2015) 4483–4488, https://doi.org/10.1016/j.matpr.2015.10.056.

[36] B.W. Chieng, Y.Y. Loo, Synthesis of ZnO nanoparticles by modified polyol method, Mater. Lett. 73 (2012) 78–82, https://doi.org/10.1016/j.matlet.2012.01.004.

[37] M.H. Livage, C. Sanchez, Sol-gel chemistry of transition metal oxide, Prog. Solid State Chem. 18 (1988) 250–341, https://doi.org/10.1016/0079-6786(88)90005-2.

[38] B.H. Toby, R.B. Von Dreele, GSAS-II: the genesis of a modern open-source all purpose crystallography software package, J. Appl. Crystallogr. 46 (2013) 544–549, https://doi.org/10.1107/S0021889813003531.

[39] H.M. Rietveld, A profile refinement method for nuclear and magnetic structures, J. Appl. Crystallogr. 2 (1969) 65–71, https://doi.org/10.1107/S0021889869006558.

[40] U. Holzwarth, N. Gibson, The Scherrer equation versus the Debye-Scherrer equation, Nat. Nanotechnol. 6 (2011) 534, https://doi.org/10.1038/nnano.2011.145.

[41] G. Xiong, U. Pal, J.G. Serrano, K.B. Ucer, R.T. Williams, Photoluminescence and FTIR study of ZnO nanoparticles: the impurity and defects perspective, Phys. Status Solidi C 3 (2006) 3577–3581, https://doi.org/10.1002/pssc.200672164.

[42] C. Kittel, Introduction to Solid State Physics, 8th ed. Willey, 2005.

[43] M. Scepanovic, M. Gruji-Brojcin, K. Vojisavljevi, S. Bernikc, T. Sreckovi, Raman study of structural disorder in ZnO nanopowders, J. Raman Spectrosc. 41 (2010) 914–921, https://doi.org/10.1002/jrs.2546.

[44] X. He, H. Yang, Z. Chen, S.S.Y. Liao, Effect of Co-doping content on hydrothermal derived ZnO array films, Physica B 407 (2012) 2895–2899, https://doi.org/10.1016/j.physb.2011.08.059.

[45] R. Zhang, P.G. Yin, N. Wang, L. Guo, Photoluminescence and Raman scattering of ZnO nanorods, Solid State Sci. 11 (2009) 865–869, https://doi.org/10.1016/j.solidstatesciences.2008.10.016.

[46] J. Tauc, Optical properties and electronic structure of amorphous Ge and Si, Mater. Res. Bull. 3 (1968) 37–46.

[47] P. Kubelka, F. Munk, Z. Tech. Phys. 12 (1931) 593–601.

[48] L.E. Brus, J. Chem. Phys. 80 (1984) 4403–4409.

[49] H.V.S. Pessoni, L.J.Q. Maia, A. Franco Jr., Mater. Sci. Semicond. Process. 30 (2015) 135–141, https://doi.org/10.1016/j.mssp.2014.09.039.

[50] M.D. McCluskey, S.J. Jokela, Defects in ZnO, J. Appl. Phys. 106 (2009), 071101. https://doi.org/10.1063/1.3216464.

[51] A.B. Djurisic, Y.H. Leung, Optical properties of ZnO nanostructures, Small 2 (2006) 944–961, https://doi.org/10.1002/smll.200600134.

[52] K. Vanheusden, W.L. Warren, C.H. Seager, D.R. Tallant, J.A. Voigt, B.E. Gnade, Mechanisms behind green photoluminescence in ZnO phosphor powders, J. Appl. Phys. 9 (1996) 7983–7990, https://doi.org/10.1063/1.362349.

[53] A. Georgea, S.K. Sharmaa, S. Chawlab, M.M. Malika, M.S. Qureshia, Detailed of X-ray diffraction and photoluminescence studies of Ce doped ZnO nanocrystals, J. Alloys Compd. 509 (2011) 5942–5946, https://doi.org/10.1016/j.jallcom.2011.03.017.

[54] H. Zeng, G. Duan, Y. Li, S. Yang, X. Xu, W. Cai, Blue luminescence of ZnO nanoparticles based on non-equilibrium processes: defect origins and emission controls, Adv. Funct. Mater. 20 (2010) 561–572, https://doi.org/10.1002/adfm.200901884.

[55] N.H. Alvi, K. Hasan, O. Nur, M. Willander, The origin of the red emission in n-ZnO nanotubes/p-GaN white light emitting diodes, Nanoscale Res. Lett. 6 (2011) 130, https://doi.org/10.1186/1556-276X-6-130.